Electronic structure of commensurate, nearly commensurate, and incommensurate phases of $1T$-TaS_2 by angle-resolved photoelectron spectroscopy, scanning tunneling spectroscopy, and density functional theory

I. Lutsyk,[1] M. Rogala,[1] P. Dabrowski,[1] P. Krukowski,[1] P. J. Kowalczyk,[1] A. Busiakiewicz,[1] D. A. Kowalczyk,[1] E. Lacinska,[2] J. Binder,[2] N. Olszowska,[3] M. Kopciuszynski,[4] K. Szalowski,[1] M. Gmitra,[5] R. Stepniewski,[2] M. Jalochowski,[4] J. J. Kolodziej,[3] A. Wysmolek,[2] and Z. Klusek[1,*]

[1]*Department of Solid State Physics, Faculty of Physics and Applied Informatics, University of Lodz, Pomorska 149/153, 90-236 Lodz, Poland*
[2]*Institute of Experimental Physics, Faculty of Physics, University of Warsaw, Pasteura 5, 02-093 Warsaw, Poland*
[3]*Faculty of Physics, Astronomy, and Applied Computer Science, Jagiellonian University, Lojasiewicza 11, 30-348 Krakow, Poland*
[4]*Institute of Physics, Maria Curie-Sklodowska University, Plac Marii Curie-Sklodowskiej 1, 20-031 Lublin, Poland*
[5]*Department of Theoretical Physics and Astrophysics, Institute of Physics, Faculty of Science, P. J. Šafárik University, Park Angelinum 9, 040 01 Košice, Slovakia*

(Received 14 March 2018; revised manuscript received 13 September 2018; published 19 November 2018)

The electronic structure of $1T$-TaS_2 showing a metal-insulator transition and a sequence of different charge density wave (CDW) transformations was discussed in the frame of variable temperature angle-resolved photoelectron spectroscopy (ARPES), scanning tunneling spectroscopy (STS), and density functional theory (DFT) calculations. For the commensurate charge density wave phase (CCDW) the Mott gap was estimated to be 0.4 eV and energy gaps $\Delta_{CCDW,1}$, $\Delta_{CCDW,2}$, $\Delta_{B3\text{-}HHB}$, $\Delta_{B4\text{-}B3}$ were observed. For the nearly commensurate charge density wave phase (NCCDW), the reminiscent of higher and lower Hubbard bands and a very pronounced electronic state associated with the parabolic band at the $\bar{\Gamma}$ point in the Brillouin zone were identified. The incommensurate charge density wave phase (ICCDW) showed a high value of local density of states at the Fermi level and a very pronounced edge of the metallic surface state located in the range of 0.15–0.20 eV above the Fermi level. The obtained STS and ARPES results were consistent with our theoretical calculations performed within DFT formalism including spin-orbit coupling.

DOI: 10.1103/PhysRevB.98.195425

I. INTRODUCTION

Transition metal dichalcogenides (TMDCs) belong to the class of materials with general formula MX_2, where M denotes a transition metal element from group IV (Ti, Zr, Hf), V (V, Nb, Ta), or VI (Cr, Mo, W), while X denotes a chalcogen atom (S, Se, Te) [1]. A polytype of TaS_2 exhibits tetragonal symmetry accompanied with octahedral coordination of the Ta atom ($1T$-TaS_2) [2]. Among all the TMDCs, $1T$-TaS_2 shows the richest phase diagram, including a pronounced metal-insulator transition (MIT) and a sequence of different charge density wave (CDW) transformations.

The phase transitions of $1T$-TaS_2 express themselves by a temperature-dependent behavior of electronic and physical properties. An undistorted normal phase of $1T$-TaS_2 exists in the temperature range of 570–550 K. Upon lowering the temperature an incommensurate CDW ordering (ICCDW, known as T_1) is observed below 550 K and then a nearly commensurate phase (NCCDW, known as T_2) at about 350 K. Finally, a commensurate (CCDW, known as T_3) ground state is reached at 180 K. When temperature is increasing transformation from CCDW to NCCDW appears at the temperature higher than 180 K; i.e., a hysteretic behavior is observed. The CCDW phase shows a $(\sqrt{13} \times \sqrt{13})R13.9^\circ$ superlattice composed of units comprising 13 tantalum atoms with a Star of David–like arrangement. The star arises when 12 Ta atoms contract towards the central Ta atom with very high displacement, all remaining in the same plane, while the neighboring S atoms, located out of the plane, undergo only minor displacements. The NCCDW phase is usually thought of as a nearly hexagonal arrangement of the Mott insulating CCDW domains separated by a metallic ICCDW network. In contrast to the CCDW phase having $(\sqrt{13} \times \sqrt{13})R13.9^\circ$ symmetry, the ICCDW phase is not rotated and shows $(\sqrt{13} \times \sqrt{13})$ reconstruction.

The $5d$ orbitals of $1T$-TaS_2 split into a lower-energy trifold-degenerate t_{2g} manifold and an upper-energy twofold e_g manifold. The triplet t_{2g} forms three subbands derived from the d_{z^2} and $d_{x^2-y^2}$, d_{xy} orbitals, while the e_g doublet forms the d_{xz}, d_{yz} subbands [3]. In the undistorted phase, the Fermi level of $1T$-TaS_2 is located in the middle of the half-filled d_z^2 band. The formation of the CDW is accompanied with splitting of the d_{z^2} band into three subbands separated by energy gaps. Two of the subbands are completely filled, while the third one is only partially filled, determining the Fermi level position [3].

Electronic band structure of $1T$-TaS_2 has been experimentally studied using angle-resolved photoemission spectroscopy (ARPES) [4–16] and angle-resolved inverse photoemission spectroscopy (ARIPES) [3,17] for both low and elevated temperatures. Particularly, for the CCDW phase,

*zbklusek@uni.lodz.pl

ARPES showed splitting of the 5*d* band into multiple subbands accompanied with the Mott-Hubbard gap opening below the Fermi level [3,17], while the absence of the energy gap was observed for the NCCDW and ICCDW phases [13]. Detailed evolution of electronic states below the Fermi level at 30 K showed two states located at about 0.4 and 0.2 eV. The binding energy of the first state decreases when the temperature is rising, and at 300 K equals 0.3 eV [13]. The second state at 0.2 eV is due to the Mott-Hubbard transition and is ascribed to the lower Hubbard band (LHB). The intensity of this state decreases with increase in temperature, and the state disappears completely above 250 K [13]. Apart from dispersion relations, also the measured Fermi maps for energies just below the Fermi level showed characteristic electron pockets for the CCDW, NCCDW, and ICCDW phases [2,5,10,11,13]. The amount of available ARIPES experimental data is limited [3,17]. Briefly, electronic states are observed at about 0.7, 2.1, and 3.7 eV above the Fermi level for the CCDW phase. The 0.7 eV state is ascribed to the upper Hubbard band (UHB). ARIPES and ARPES give the energy gap of about 400 meV and the Fermi level in the middle of the gap [17].

The $1T$-TaS_2 electronic structure was also studied by the use of scanning tunneling microscopy/spectroscopy (STM/STS). Clean samples [18], doped samples [19,20], and nanoscale manipulation of the Mott insulating state with the STM tip were investigated [21,22]. However, to our best knowledge, these studies were carried out at low temperatures; thus they were restricted mainly to the CCDW phase.

To form a better view of the electronic structure of $1T$-TaS_2, we have investigated it within the scope of high, room, and low temperatures for the presence of three phases, i.e., ICCDW, NCCDW, and CCDW. This paper provides a comprehensive study by experimental techniques such as STM/STS, ARPES, and low-energy electron diffraction (LEED) together with theoretical calculations using density functional theory (DFT). Our STS measurements have been performed up to high temperatures, resulting in a more extended data set, as previous studies were restricted mainly to low temperatures. One remaining data set involves experiments at high temperatures, which raises further difficulties in the measurement process. Understanding the $1T$-TaS_2 electronic structure will enhance future investigations of properties of graphene/TaS_2 hybrids at different temperatures. In these systems, it is expected that graphene/TaS_2 interaction would be observed not only for metallic but also for insulating states due to MIT transition. Furthermore, the presence of different lattice distortions of TaS_2 will enable the control of interlayer orientation between two materials forming the graphene/TMDC hybrid system, thus affecting graphene electronic structure. The synergistic properties of hybrid systems promise potential in various electronic applications. However, the first crucial step is to know the electronic structure of $1T$-TaS_2 for different phases, particularly at the nanometer scale as described in this study.

II. METHODS

All the STM/STS and LEED measurements were carried out inside the Multiprobe P (Scienta Omicron) system in UHV under the base pressure of 3×10^{-10} mbar. The STM and STS results were collected by VT STM/AFM microscope (Scienta Omicron) at 110, 293, and 400 K. The STM tips were prepared by mechanical cutting of the 90%Pt–10%Ir alloy wires (Goodfellow). In the current imaging tunneling spectroscopy mode (CITS) the *I*/V curves were recorded simultaneously with a constant current image by the use of the interrupted-feedback-loop technique. Based on these measurements the first derivative of the tunneling current with respect to voltage (dI/dV) was calculated. LEED data were acquired by an OCI Vacuum Microengineering Inc. spectrometer at 110, 293, and 400 K with energy set to 95 eV.

The ARPES measurements were performed by two independent systems. The first system was equipped with a SPECS UVS-300 photon source (HeI/HeII) and Specs Phoibos 150 hemispherical energy analyzer associated with a multichannel plate detector (MCP). The energy and angular resolution were set to 40 meV and 0.5°, respectively. The second system was equipped with a high-brightness lamp Gammadata-Scienta VUV5000 (HeI/HeII) with monochromator Gammadata-Scienta VUV5040 and hemispherical Gammadata-Scienta R4000 WAL analyzer. The energy and angular resolution were 10 meV and 0.5°, respectively. In both systems, the HeI α line (21.23 eV) was used to excite photoelectrons.

High-quality $1T$-TaS_2 crystals were supplied by HQ Graphene and cleaved *in situ* in UHV condition at room temperature.

Calculations of electronic properties of $1T$-TaS_2 were performed within density functional theory (DFT) formalism [23] using QUANTUM ESPRESSO software [24,25], which exploits a plane-wave basis set and utilizes the pseudopotential approach. The fully relativistic pseudopotentials, projector augmented wave method [26], and revised Perdew-Burke-Ernzerhof generalized gradient approximation [27] were used to include the exchange and correlation effects. The spin-orbit coupling was fully taken into account. In the absence of periodic lattice distortion (PLD), the calculations were carried out for the presence of 100 bands with experimental lattice constants taken from Ref. [28]. The kinetic energy cutoff was set to 53 Ry for wave functions and 402 Ry for charge density, respectively, while the energy convergence threshold for self-consistency amounted to 10^{-8} Ry. The self-consistent calculations were preceded by relaxation of atomic positions in the unit cell (until the total force was below 10^{-6} Ry/bohr) yielding the S atoms shift of ± 0.2566 (relative to the lattice constant c) with respect to the plane containing Ta atoms, which agrees with the experimental value of ± 0.2586 [28]. The relaxation and self-consistent calculations used a Monkhorst-Pack mesh of $32 \times 32 \times 20\,k$ points, whereas DOS calculations were done for a denser mesh of $48 \times 48 \times 24$ k points. For comparison, the calculations excluding spin-orbit coupling (SOC) revealed a noticeable impact of SOC on the band structure of $1T$-TaS_2. In the presence of PLD, the calculations in a $(\sqrt{13} \times \sqrt{13})R13.9°$ supercell were performed starting from the experimental PLD positions of atoms taken from Ref. [28] on the mesh of $6 \times 6 \times 12\,k$ points with 400 bands. It was found that the relaxation finished at positions considerably close to the starting (experimental) positions, proving the stability of the PLD. The total energy of the phase with PLD per TaS_2 was found to be approximately

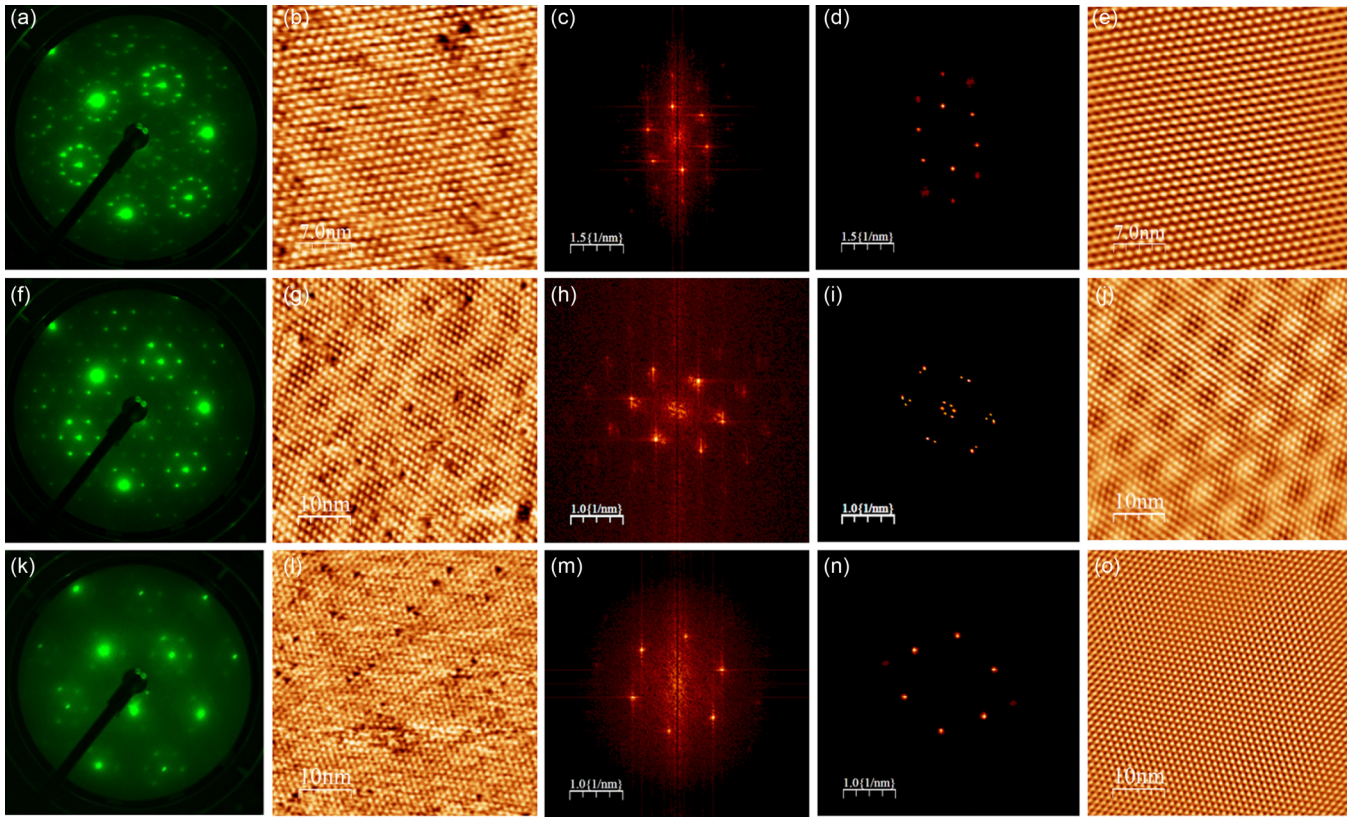

FIG. 1. LEED patterns, raw STM topographies, FFT power spectra of the raw STM topographies, selected frequencies for the calculation of the FFT filtered topographies, and Fourier filtered STM topographies for the UHV cleaved $1T$-TaS_2 sample: (a)–(e) the CCDW phase at 110 K; (f)– (j) the NCCDW phase at 293 K; (k)–(o) the ICCDW phase at 400 K.

25 meV lower than the energy of the undeformed phase. It should be emphasized that the only phase with PLD accessible for DFT calculations is the CCDW phase (the other, noncommensurable phases would require excessively large supercells to enforce periodicity, which is necessary for the calculations). The fast Fourier transform (FFT) power spectra of the raw STM topographies were calculated using WSXM 5.0 DEVELOP 7.0 software [29].

III. RESULTS AND DISCUSSION

A. Low-energy electron spectroscopy and scanning tunneling microscopy measurements

The investigated $1T$-TaS_2 samples were initially characterized using temperature-dependent Raman scattering and electrical experiments. The Raman scattering showed that our samples exhibit similar behavior to those previously observed in many experiments [30–32]. The measured temperature dependence of electrical resistivity resembles the results obtained by other researchers [33–35] and also confirms the presence of phase transitions typical for $1T$-TaS_2.

In Fig. 1(a) we show the LEED pattern and in Fig. 1(c) the FFT power spectrum of the raw STM topography [Fig. 1(b)] of the CCDW phase recorded at 110 K for the UHV cleaved $1T$-TaS_2 sample. The LEED pattern shows six well pronounced atomic-lattice Bragg spots. Each spot is surrounded by twelve satellite spots, which can be grouped into two separate hexagons. The appearance of the satellite spots is not confirmed by the FFT power spectrum of the raw STM topography [Fig. 1(c)]. However, it should be emphasized that LEED is a global technique, which provides us with data averaged over some surface area that may belong to different domains on the surface. As a result, a superposition of different patterns might be expected. This is not the case of local STM technique, where data are collected from the nanometer-scale area leading to the much simpler power spectrum. The measured distance between Bragg spots is equal to $0.8\,\mathrm{nm}^{-1}$, which gives the distance of 1.25 nm in the real space. This value is typical for the distance between so-called Stars of David forming a commensurate $(\sqrt{13}\times\sqrt{13})R13.9^\circ$ superlattice with a measured period of about 1.25 nm. Taking into account pronounced maxima of the FFT power spectrum [Fig. 1(d)], we calculated Fourier filtered STM topography [Fig. 1(e)], which shows regular CDW bright features. Each feature consists of 13 Ta atoms arranged into a Star of David forming a commensurate $(\sqrt{13}\times\sqrt{13})R13.9^\circ$ superlattice with a measured period of about 1.25 nm. The angle between the CCDW unit cell and unreconstructed atomic lattice estimated from our LEED and high-resolution STM topography is equal to 13.8° and 13.6°, respectively (see Figs. S1(a), S1(b), and S2(a) in the Supplemental Material [36]).

The LEED pattern, raw STM topography, and FFT power spectrum recorded for the NCCDW phase (293 K) are presented in Figs. 1(f)–1(h), respectively. The LEED pattern shows well separated atomic-lattice Bragg spots each surrounded by six PLD satellite spots. The spots are rotated by an

angle of about 11.9° with respect to the lattice (see Figs. S1(c) and S1(d) in the Supplemental Material [36]), which is in good accordance with the previous measurements [37–42]. Also, there are visible traces of higher-order diffraction spots, which can be ascribed to the presence of a domainlike structure of the NCCDW phase. However, instead of closely spaced higher-order maxima reported by ultrafast low-energy electron diffraction (ULEED) studies [36], we observe spots with a rather smeared ellipsoidal shape. The LEED pattern can be directly compared with the FFT power spectrum [Fig. 1(h)] of the raw STM topography [Fig. 1(g)]. The FFT power spectrum shows six spots with a high intensity, which are related to the Bragg spots. The six spots form a slightly distorted hexagon with the distance between spots of 0.7 and 0.9 nm^{-1}. These values are related to the distances in the real space equal to 1.42 and 1.1 nm, respectively. The spots correspond to the presence of Stars of David and the small distortion is most likely caused by thermal drift. Furthermore, each Bragg spot is surrounded by PLD satellite spots. However, instead of six satellites typical for LEED pattern, we observe one or two spots only. The limited number of observed PLD satellites on the FFT power spectrum is caused by the fact that the CDW amplitude modulation envelope is not purely sinusoidal as was reported previously [38]. Like in the case of LEED, we also observe smaller hexagonal arrangements of spots in the very center of the FFT power spectrum. This is a direct indication of the periodic modulation of the CDW forming domains with relatively high amplitude. The measured distance between spots ranges from 0.16 nm^{-1} up to 0.135 nm^{-1}, which results in the domain period from 6.25 to 7.40 nm in the real space. This value is in good accordance with the previous measurements [38–42]. Taking into account six Bragg spots together with visible satellite spots and the lowest-order spots forming the central hexagon of the FFT power spectrum [as shown in Fig. 1(i)] it is possible to calculate Fourier filtered STM topography presented in Fig. 1(j).

Within commonly accepted models, the NCCDW phase consists of a hexagonal array of commensurate domains with relatively high amplitude separated by domain walls in which amplitude is lower [38–42]. It results in STM topographies showing a hexagonal array of bright domains separated by darker walls as presented in Fig. 1(j). However, it should be highlighted that the STM topographies of NCCDW presented in the literature vary essentially. This variation comes from the fact that different discrimination levels of the topography signal or different frequencies for the calculation of the FFT filtered STM image may be chosen in order to enhance the presence of domains. Furthermore, the domain intensity, shape, and distribution on the surface strongly depend on temperature [41,42]. That is why the STM topography presented in Fig. 1(j) should be treated as an example chosen from the set of NCCDW topographies. Moreover, in Figs. 2(a)–2(d) we show higher magnification of the STM topographies together with FFT power spectra. In Fig. 2(a) we see the topography of the NCCDW phase, which shows a rather irregular distribution of relatively bright regions (domains) separated by darker regions (domain walls). The lack of periodic arrangements of bright domains is clearly confirmed by the FFT power spectrum [Fig. 2(b)], which does not show six spots with the hexagonal arrangement in the very center of the FFT image. Instead of that a smeared area of frequencies is observed.

In Figs. 2(c) and 2(d) we present high-resolution STM topography together with a FFT power spectrum. On the STM topography, it is easy to resolve small regions with high brightness ascribed to domains (marked by black lines) separated by darker regions corresponding to the domain walls. The presented topography is in good accordance with a model assuming that the NCCDW phase consists of the arrangement of the Mott insulating CCDW domains separated by a metallic ICCDW network. The estimated angle between the Stars of David in the domains and unreconstructed atomic lattice equals 11.5°(see Fig. S2(b) in the Supplemental Material [36]). Furthermore, the shape of the Stars of David in the domains proves the large contribution of the central Ta-$5d_{3z^2-r^2}$ orbital to the electron local density of states (LDOS) and a small contribution of the orbitals at the edges of the stars [43]. This is particularly confirmed by FFT filtered high-resolution STM topography [Fig. 2(e)] together with our DFT calculation of LDOS presented in Figs. 2(f)–2(h). Since our STM topographies were acquired at very low negative bias voltages, it is justified to compare the topography presented in Fig. 2(e) with the LDOS map calculated at the Fermi level shown in Fig. 2(f). The obtained STM topography and theoretical DFT result are in good accordance.

The LEED pattern, raw STM topography, and FFT power spectrum recorded for the ICCDW phase (400 K) are presented in Figs. 1(k)–1(m), respectively. On the ICCDW phase, LEED reveals a much less intense pattern both for atomic-lattice Bragg and for PLD satellite spots; see Fig. 1(k). The higher-order diffraction spots for the ICCDW phase are not observed due to the weak PLD as stated previously [37]. What is important is that we do not observe (or it is really difficult to observe) hexagonal arrangements of spots in the very center of the LEED pattern. This is a direct indication that we cannot expect the periodic modulation of the CDW, which forms domains like in the case of the NCCDW phase. This is confirmed by the FFT power spectrum [Fig. 1(m)] of the raw STM topography [Fig. 1(l)]. However, it is easy to observe six spots with a high intensity related to the Bragg spots. The six spots form a slightly distorted hexagon with the measured distance between spots in the range of 0.875–0.964 nm^{-1} giving the distances in the real space from 1.14 to 1.04 nm. Taking into account high-intensity spots [Fig. 1(n)], we calculated Fourier filtered STM topography [Fig. 1(o)], which shows regularly arranged bright features with a measured period of about 1.04–1.14 nm. As expected from the LEED and FFT analysis no trace of any domain structure is observed. Higher magnification of STM topographies together with FFT power spectra are presented in Figs. 2(i)–2(l). With the aid of STM topography profiles and FFT power spectra, we measured that the distance between bright features varies from 0.94 to 1.17 nm. We ascribed the observed bright features to the presence of diffused spots detected in an x-ray diffraction experiment [28]. The positions of these spots are defined by an incommensurate wave vector equal to $q_i = 0.283a_0^* + \frac{c_0^*}{3}$, where a_0^* and c_0^* are reciprocal wave vectors. The wavelength between CDW maxima is equal to $\lambda = \frac{2\pi}{q_{isurf}}$, where $q_{isurf} = 0.283a_0^*$, $a_0^* = \frac{2}{\sqrt{3}}\frac{2\pi}{a}$, $a = 0.336\,49$ nm. This gives

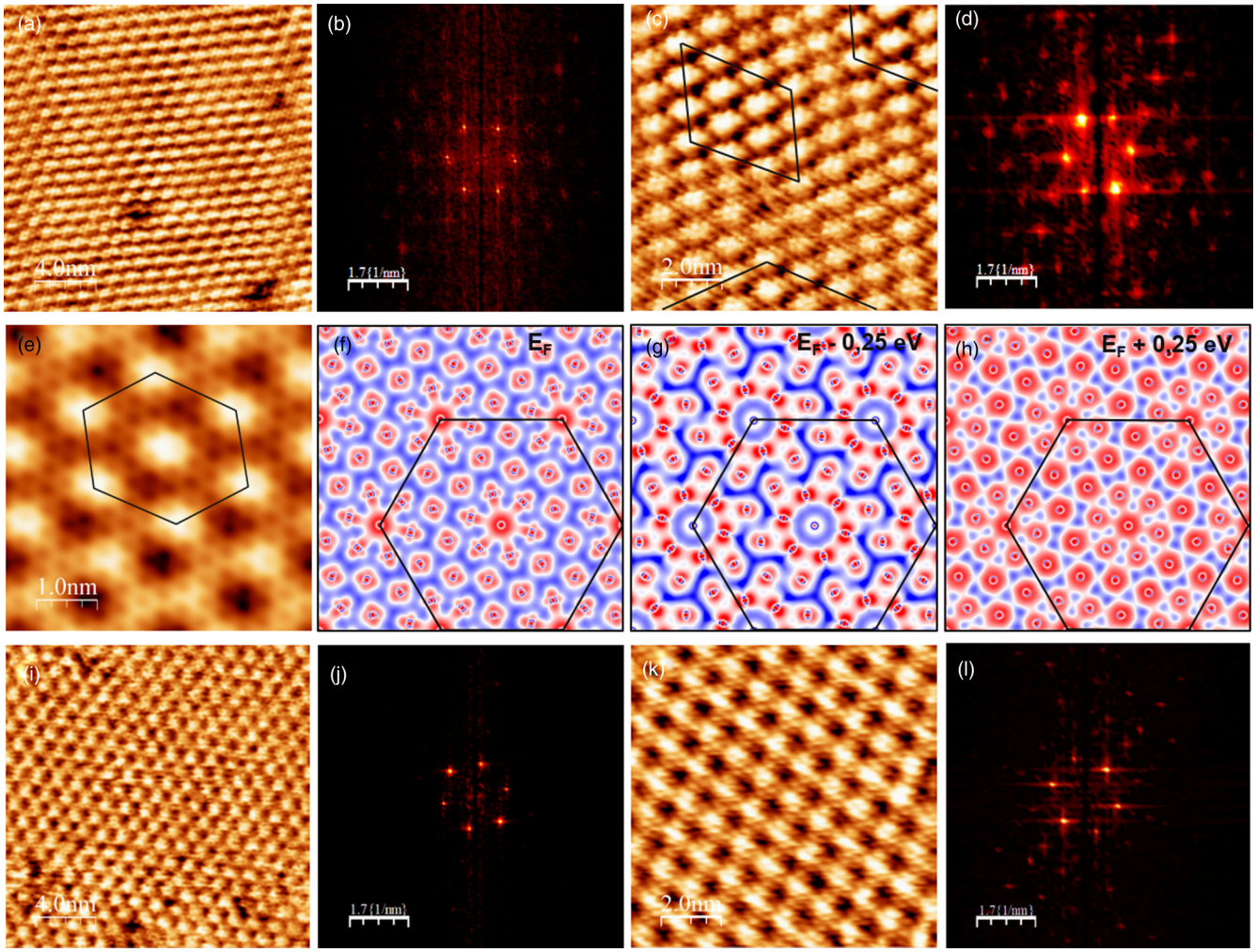

FIG. 2. (a)–(d) Raw STM topographies and FFT power spectra for the UHV cleaved $1T$-TaS_2 sample at 293 K. (e) High-resolution FFT filtered STM topography for the $1T$-TaS_2 sample at 293 K. (f)–(h) DFT maps of electron density of states calculated for different energies relative to the Fermi level for the CCDW phase. (i)–(l) Raw STM topographies and FFT power spectra for the UHV cleaved $1T$-TaS_2 sample at 400 K.

the distance between CDW maxima equal to 1.029 nm, which is in good accordance with our STM results. As expected for the ICCDW phase the estimated angle between CDW modulations and the unreconstructed atomic lattice equals 0°(see Figs. S1(e), S1(f), and S2(c) in the Supplemental Material [36]). Unfortunately, in the case of the ICCDW phase, we are not able to calculate the LDOS map, which could be directly compared with the STM topographies. This is because the analysis of ICCDW is far beyond the possibilities of DFT being essentially rather a ground-state tool; thus we do not attempt to construct a DFT-based model for that.

The LEED/STM results clearly show the existence of the CCDW, NCCDW, and ICCDW phases at 110, 293, and 400 K, respectively. Our STM results for the CCDW phase are in good accordance with previously published data for this phase. The STM topographies for the NCCDW phase agree with a commonly accepted model with domain/wall structure constituting this phase. Furthermore, the domain structure recorded by STM agrees with LDOS maps obtained by our DFT calculations. The STM results for the ICCDW phase are in good accordance with previously published x-ray diffraction experiments. The obtained topographic results enable us to carry out spectroscopy measurements, particularly at high temperature, and elucidate the electronic structure of the measured phases.

B. Angle-resolved photoemission spectroscopy measurements

Figures 3(a)–3(c) show ARPES band dispersion relation of $1T$-TaS_2 measured along the $\bar{\Gamma} - \bar{M}$ direction at the three different phases, i.e., CCDW (130 K), NCCDW (293 K), and ICCDW (400 K). The data were recorded with 40 meV/0.5° (energy/angular) resolution. For the CCDW phase (at 130 K), the following are seen: the Ta $5d$–derived bands extending down to around −1.2 eV below the Fermi level (E_F) and the S $3p$–derived bands at higher binding energies. The Ta $5d$ band splits into three submanifolds denoted by the LHB, B1, B2, separated by energy gaps. The LHB is observed around the $\bar{\Gamma}$ point close to the Fermi level. The photocurrent signal is suppressed between the Fermi level and the LHB constituting an insulating energy gap. This gap is ascribed to the half width

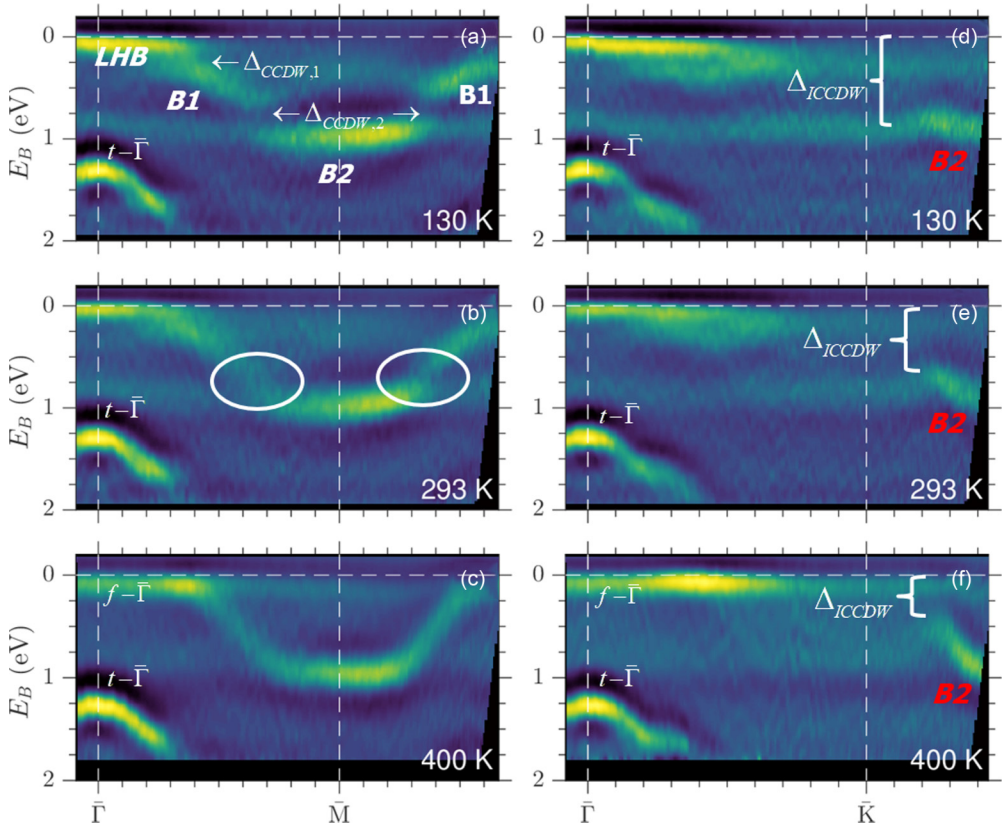

FIG. 3. ARPES measurements recorded at three different phases of $1T$-TaS_2 measured along the $\bar{\Gamma}-\bar{M}$ and $\bar{\Gamma}-\bar{K}$ directions [see Fig. 4(f) for indication of the direction]. (a), (d) The CCDW phase at 130 K; (b), (e) NCCDW at 293 K; (c), (f) ICCDW at 400 K. The gaps denotation is taken from the paper given by Sohrt *et al.* [15].

of the Mott gap $\frac{1}{2}\Delta_{\text{Mott}}$ and it is read as ∼0.2 eV (see also Fig. S2 in the Supplemental Material for higher-resolution ARPES data [36]). The next two gaps: $\Delta_{\text{CCDW},1}$ and $\Delta_{\text{CCDW},2}$, are related to the presence of the CDW in the commensurate phase; they are equal to 0.23 and 0.35 eV, respectively. The characteristic features are in accordance with the previous ARPES data given in Refs. [2,9,13,14,16]. When the temperature reaches 293 K, which is typical for the existence of the NCCDW phase, the splitting of the Ta $5d$ band is hardly observable. Nevertheless, one is still able to see a decrease of the photocurrent signal reminiscent of energy gaps as marked by the elliptical circles in Fig. 3(b). Finally, when temperature increases to 400 K (the ICCDW phase) the splitting of the Ta $5d$ band disappears completely; see Fig. 3(c).

Similar ARPES measurements were performed along the $\bar{\Gamma}-\bar{K}$ direction, which are presented in Figs. 3(d)–3(f). Similar to the case of band dispersion along the $\bar{\Gamma}-\bar{M}$ direction it is possible to clearly observe parabolic band structure at the $\bar{\Gamma}$ point with a maximum at about −1.3 eV ($t-\bar{\Gamma}$), which does not strongly depend on temperature. When moving from the $\bar{\Gamma}$ point towards the $\bar{K}$ point we observe a lack of any bands between −0.15 and −1.3 eV. However, after passing the $\bar{K}$ point we begin approaching the $\bar{M}$ point; see Fig. 4(f) for the surface Brillouin zone scheme. As a consequence, the band B2 starts to appear. The energy gap between the Fermi level and the top of the B2 band is denoted as Δ_{ICCDW} [15]. The inspection of Figs. 3(d)–3(f) clearly shows that the width of the Δ_{ICCDW} decreases when temperature is increasing; also the intensity of the B2 band appears to be higher at elevated temperatures.

In Fig. 4 we present combined ARPES measurements carried out along the $\bar{\Gamma}-\bar{M}$ and $\bar{\Gamma}-\bar{K}$ directions together with our DFT calculations. The band structure calculation for the bulk $1T$-TaS_2 including PLD [inducing the $(\sqrt{13}\times\sqrt{13})R13.9^\circ$ reconstruction reflected by selection of the supercell] and SOC are presented in Figs. 4(d) and 4(e). It should be emphasized here that for $1T$-TaS_2, being a quasi-two-dimensional electron system, one can directly compare the ARPES spectra and the theoretically calculated dispersion relations. This conclusion is based on the variable photon energy ARPES studies finding immobile characteristic spectral features vs photon energy, which indicates clearly that the $k_\perp$ is not the relevant quantum number for this system [44]. The calculations are representative for the CCDW phase. They show that the CCDW phase behaves as an insulator with the in-plane energy gap of around 0.4 eV; see Fig. 4(d). Also, they show that the CCDW exhibits metallic properties in the out-of-plane direction, i.e., $\Gamma-A$ [Fig. 4(e)].

The overall band shapes revealed by ARPES at 400 K [Fig. 4(c)] are in accordance with our theoretical model for bulk $1T$-TaS_2 without PLD. Due to the fact that at higher temperatures the PLD is reduced compared to the CCDW phase, the theoretical results are suitable for the description of the ICCDW phase [see Figs. 4(i) and 4(j)]. The calculated band structure presented in Figs. 4(i) and 4(j) includes SOC. The ICCDW phase is metallic in the in-plane directions; see

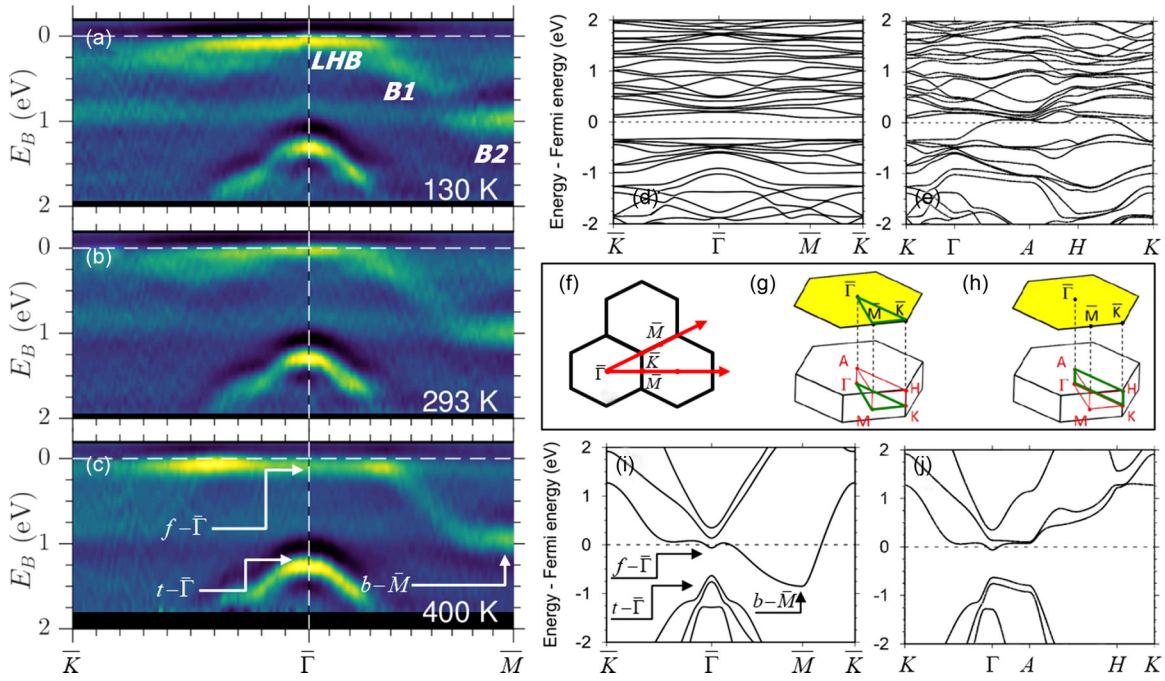

FIG. 4. ARPES measurements recorded at three different phases of $1T$-TaS_2 measured along the $\bar{K}-\bar{\Gamma}-\bar{M}$ direction. (a) The CCDW phase at 130 K; (b) NCCDW at 293 K; (c) ICCDW at 400 K. (d), (e) Band structure calculated for bulk $1T$-TaS_2 with PLD representative for the presence of the CCDW phase. (f)–(h) Surface and bulk Brillouin zones of $1T$-TaS_2 with marked high-symmetry points. (i,j) Band structure calculated for bulk $1T$-TaS_2 without PLD representative for the presence of the ICCDW phase.

Fig. 4(i). However, it behaves as an insulator with the out-of-plane direction; i.e., along $\Gamma - A$ it shows a band gap of ∼0.5 eV; see Fig. 4(j). This is opposite to the case of the CCDW phase showing metallic properties in the out-of-plane direction and insulating behavior in plane. The calculations performed without and with SOC revealed noticeable importance of the SOC factor in shaping the band structure, in the vicinity of the Fermi level in the $1T$-TaS_2. In particular, in the vicinity of the $\bar{\Gamma}$ point, SOC induces splitting in the conduction band with the mutual distances between three bands of the order of 0.20 eV, while in the valence band the corresponding splitting value between the upper and lower band reaches 0.13 eV. Moreover, the lower branch of the SOC-split conduction band is pushed down so that it crosses the Fermi level close to $\bar{\Gamma}$ in total three times along the $\bar{K}-\bar{\Gamma}-\bar{M}$ direction. In spite of the noticeable influence of SOC on the bands in the vicinity of the Fermi level, the gap value at the $\bar{\Gamma}$ point is only slightly varied under the influence of SOC and amounts to 0.56 eV. The comparison of the high-temperature ARPES data with DFT calculations along the $\bar{\Gamma}-\bar{M}$ and $\bar{\Gamma}-\bar{K}$ directions [Figs. 4(c) and 4(i)] reveals the presence of a relatively flat band ($f-\bar{\Gamma}$) close to the Fermi level. The band falls down halfway to the $\bar{M}$ point ($b-\bar{M}$). The calculations show also that the band is lifted up when approaching the $\bar{K}$ point (not reflected in ARPES data limited to $E_B \leqslant 0$). A valence band derived from S $3p$ states is also well pronounced with its maximum at the $\bar{\Gamma}$ point ($t-\bar{\Gamma}$). When tending from $\bar{\Gamma}$ to $\bar{K}$ [Fig. 4(c)] the arm of the valence band broadens significantly below some energy, as seen also in the DFT calculations [Fig. 4(i)]. This takes place close to the anticrossing of the upper and lower band seen in Fig. 4(i). A trace of such behavior, i.e., broadening, is observable for phases at lower temperatures as well.

It is worth remembering that the temperature induces smearing of the Fermi-Dirac distribution and leads to a redistribution of the electrons into states that are empty at a lower temperature. As a result, it is possible to carry out ARPES measurements even up to 5 kT above the Fermi level with a HeI α radiation source [45]. It gives a possibility of observing electronic states at energies of 56, 126, and 172 meV above the Fermi level at temperatures: 130, 293, and 400 K, respectively. The representative results recorded very close to the Fermi level in the form of $E(k_x, k_y)$ maps at different temperatures are shown in Fig. 5. For the sake of clarity, we analyzed the $E(k_x, k_y)$ maps in the vicinity of the $\bar{\Gamma}$ point, fixing $k_y = 0$ simultaneously.

It is clear that the intensity of the signal below the Fermi level is much higher at 130 and 293 K than the signal recorded at a temperature of 400 K. This is because at high temperature, electrons from occupied states are excited to unoccupied states above the Fermi level, decreasing the signal yield. For the CCDW, NCCDW, and ICCDW phases we also observe a signal just above the Fermi level, which means that the energy bands must exist at the $\bar{\Gamma}$ point for unoccupied states. In the case of the CCDW phase, that fact is confirmed by tight-binding calculation (TB) [7], the full-potential linearized augmented-plane-wave (FLAPW) method [7], and ARIPES data [17]. The DFT and ARPES data confirm the existence of the band above the Fermi level for the NCCDW phase [8,10]. Finally, the existence of the band at the $\bar{\Gamma}$ point for the ICCDW is proved by TB [15] and our DFT calculations, which are shown in Fig. 4(i). It is worth noting that above the Fermi level

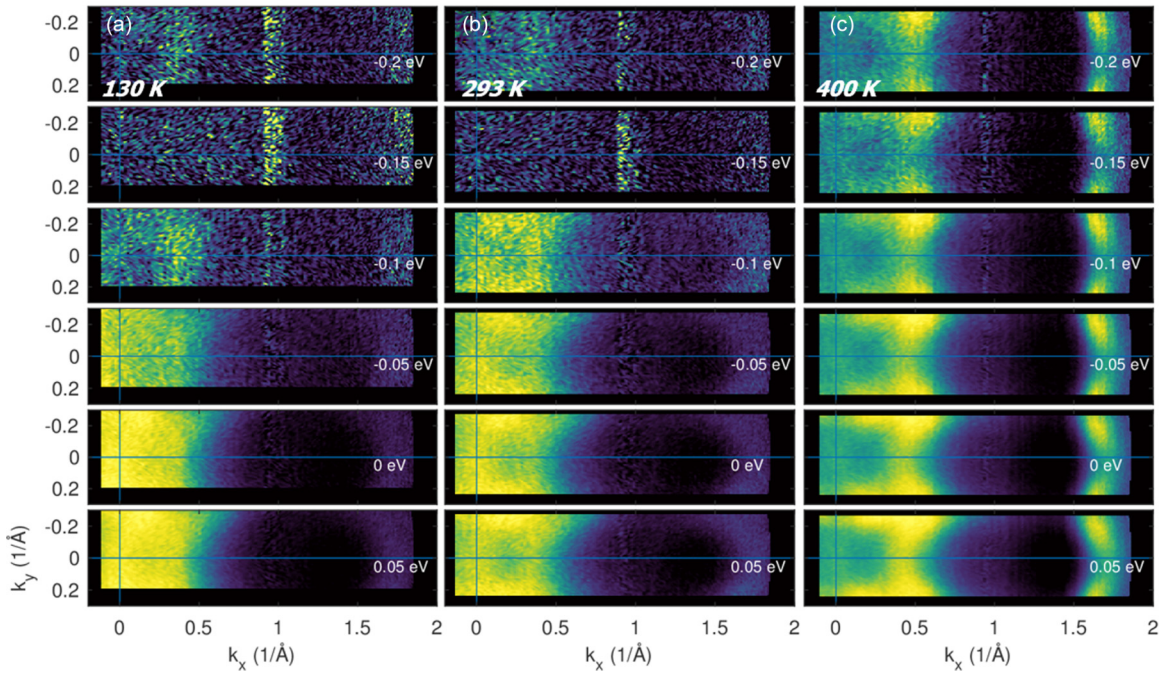

FIG. 5. ARPES measurements in the form of $E(k_x, k_y)$ maps at different temperatures and energies grouped into three columns. Column (a) temperature 130 K; column (b) temperature 293 K; column (c) temperature 400 K. k_x span along the $\bar{\Gamma} - \bar{M}$ direction. Energy relative to the Fermi level is labeled at each map. Negative energies mean electronic states above the Fermi level.

the intensity of the signal decreases rapidly at temperatures of both 130 K (starting from −0.05 eV) and 293 K (starting from −0.1 eV), which is caused by a limited number of electrons redistributed into unoccupied states at lower temperatures. This is not the case of the high-temperature ICCDW phase, where signal intensity decreases very slowly above the Fermi level due to the effective thermal excitation process.

Additionally, in Fig. 6(a) we present integrated energy distribution curves (IEDCs), which were obtained from photoemission spectra recorded at three different temperatures, i.e., 130, 293, and 400 K. Integration was performed for the wave vectors along the $\bar{\Gamma} - \bar{M}$ direction from $-0.1\,\text{Å}^{-1}$ up to $0.1\,\text{Å}^{-1}$ (see also Fig. S4 in the Supplemental Material for IEDC obtained from higher-resolution ARPES data recorded at 80 K for the CCDW phase [36]). We chose this narrow wave-vector range in order to compare our ARPES results with the STS data. The STS technique is very sensitive to electronic states located at $\overrightarrow{k_\parallel} \approx 0$ (the center of the Brillouin zone), which determines tunneling current. It leads to the situation that the surface density of states probed by STS resembles IEDCs measured for low values of the wave vector.

The obtained IEDCs clearly show pronounced peaks [occupied band (OB)] at an energy of about 1.3 eV below the Fermi level, which can be ascribed to the presence of the band maximum at the $\bar{\Gamma}$ point ($t - \overline{\Gamma}$); see Figs. 3 and 4. The position of the OB peaks does not strongly depend on temperature. This is opposite to the case of peaks located close to the Fermi level, which are ascribed to the LHB, reminiscent of the lower Hubbard band (r-LHB), and the edge of the metallic state (EMS) for the CCDW, NCCDW, and ICCDW phases, respectively. These peaks can be evidently resolved when integration process is performed for the wider range of wave vectors, from $-0.1\,\text{Å}^{-1}$ up to $1.0\,\text{Å}^{-1}$; see Fig. 6(b). One should notice that the higher the temperature is, the higher is the observed intensity of the IED signal above the Fermi level. Furthermore, the analysis of the IECDs results including comparison with the STS data will also be given in the next part, which is devoted to scanning tunneling spectroscopy measurements.

C. Scanning tunneling spectroscopy measurements

An illustrative way of presenting spatially resolved STS data is to plot the *dI*/*dV* quantity, which is a measure of local density of states (LDOS) as a function of bias voltage (closely related to energy) and position along a chosen line on the surface. We expect the STS results to be closely related to the already discussed band structure of $1T$-TaS_2 around the $\bar{\Gamma}$ point since the tunneling electrons have their k vectors preferentially not far from the normal to the surface [the effective tunneling decay constant is $\sqrt{(2\Phi_B + k_\parallel^2)/\hbar^2}$, Φ_b being the energy barrier for tunneling]. In Figs. 7(a), 7(c), and 7(e), we show LDOS maps measured along the lines with the length of 110, 50, and 20 nm, recorded on the $1T$-TaS_2 surface, for the CCDW (130 K), NCCDW (293 K), and ICCDW (400 K) phases.

Cleary, the spectra differ considerably from each other. The LDOS map recorded for the CCDW phase (130 K) shows electronic structure heterogeneity considered in terms of changes of amplitude and energy position of the LDOS features along the position on the surface. It might be caused by the presence of surface defects or regions in which coexistence of different phases takes place. On that map, we recognize low and high Hubbard bands (HHBs) separated

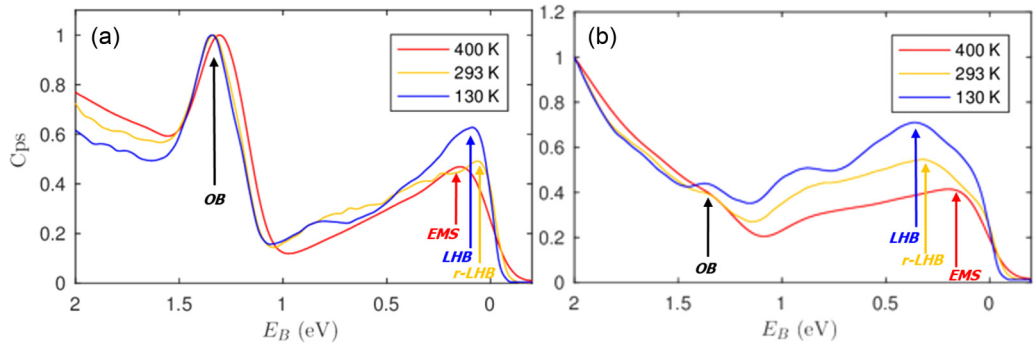

FIG. 6. Integrated energy distribution curves. (a) IEDCs for three different temperatures integrated in the wave-vector range: $-0.1\ \text{Å}^{-1}$ up to $0.1\ \text{Å}^{-1}$. (b) IEDCs for three different temperatures integrated in the wave-vector range: $-0.1\ \text{Å}^{-1}$ up to $1.0\ \text{Å}^{-1}$.

by the Mott gap Δ_{Mott}, defined as a distance between the LHB and HHB. In order to estimate the Δ_{Mott} value we take into account the *dI*/*dV* profile [see Fig. 7(b)] taken along the vertical cross section at the position marked by the arrow #1 in Fig. 7(a). Firstly, we read the distance between LHB and the Fermi level (corresponding to the bias 0 V), which equals 0.15 eV. This value is close to our ARPES measurements $\frac{1}{2}\Delta_{\text{Mott}} = 0.2$ eV and the previous ARPES data giving a value of around 0.2 eV [2,9,13,14,16]. From our STS experimental result, we can also easily read the value of Δ_{Mott} equal to 0.40 eV, which is the same as the value estimated using combined ARPES/ARIPES techniques [17]. This agreement is observed in spite of the fact that in the angle-resolved photoemission techniques the energy gap is estimated using the $E(k)$ dispersion relation, while in STS the gap is measured as a distance between maxima of LDOS. Furthermore,

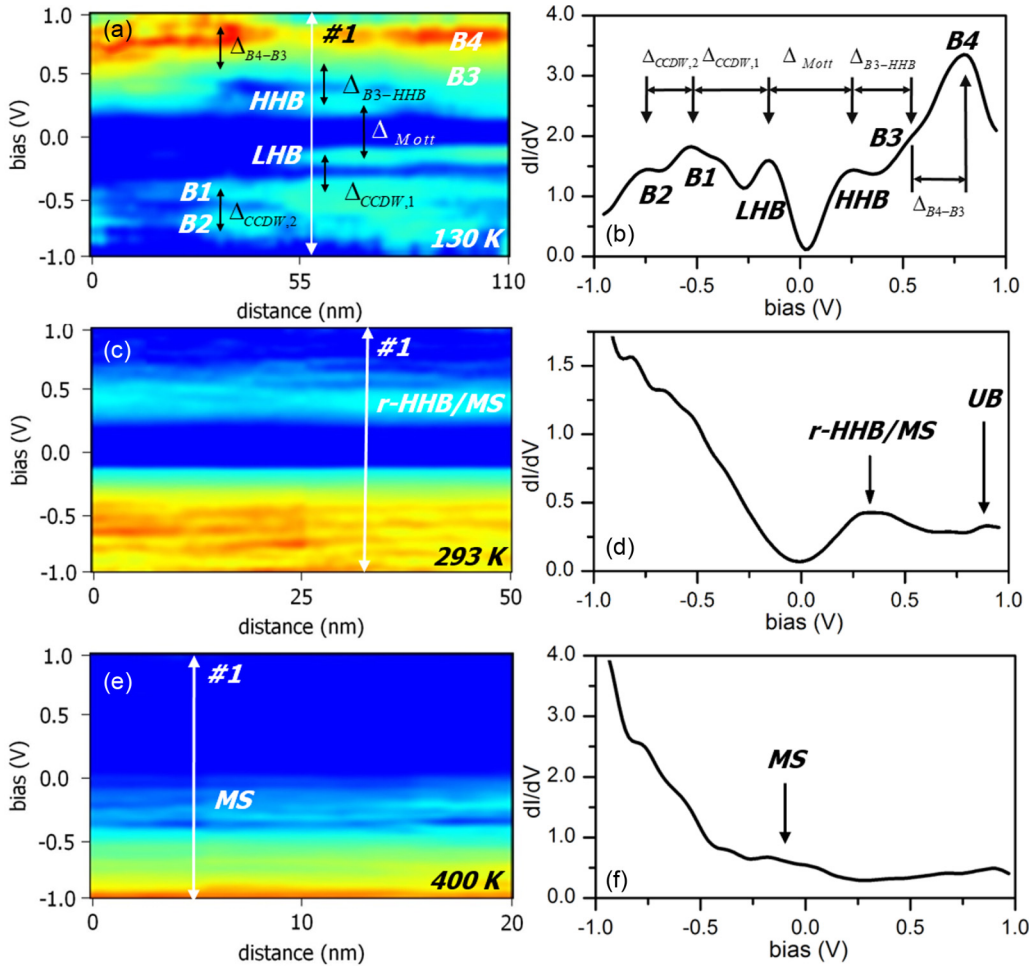

FIG. 7. LDOS maps and corresponding *dI*/*dV* profiles: (a), (b) at 130 K for the CCDW phase; (c), (d) at 293 K for the NCCDW phase; (e), (f) at 400 K for the ICCDW phase. On the LDOS map blue color corresponds to low value of LDOS, while red color corresponds to high value of LDOS.

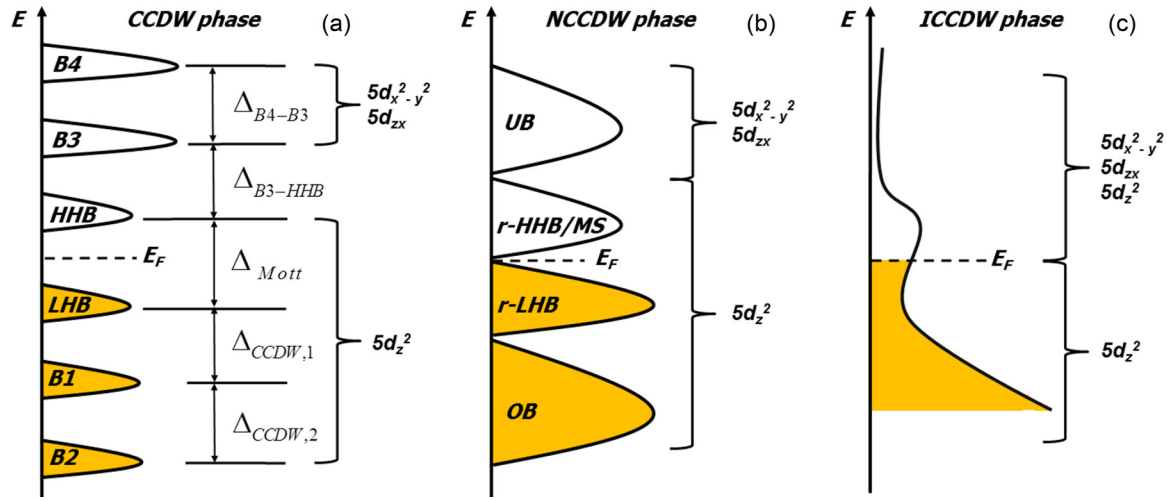

FIG. 8. Schematic model of DOS structure of the (a) CCDW, (b) NCCDW, and (c) ICCDW phases. Please note that the energy scales for CCDW, NCCDW, and ICCDW are not the same. Yellow color denotes occupied states.

it should be mentioned that the energetic resolution of the ARIPES technique is not as good as the resolution of STS and it may cause some serious problems when high accuracy is required. In this place, it is valuable to remark that Cho *et al.* [18] estimated the Δ_{Mott} as 0.32 eV using the STS technique. Moreover, they observed that the Fermi level is closer to the LHB than the HHB (what we see in our experiments, too). Apart from the position of the LHB (0.15 eV), it is also possible to estimate energy of the *B*1 (0.55 eV) and *B*2 (0.75 eV) bands and consequently the energy gaps $\Delta_{\mathrm{CCDW},1} = 0.40$ eV and $\Delta_{\mathrm{CCDW},2} = 0.20$ eV. The obtained values can be compared with the energy gaps $\Delta_{\mathrm{CCDW},1} = 0.23$ eV and $\Delta_{\mathrm{CCDW},2} = 0.35$ eV measured in our ARPES experiment and values estimated by the normalized correlation coefficient STS technique, $\Delta_{\mathrm{CCDW},1} = 0.24$ eV and $\Delta_{\mathrm{CCDW},2} = 0.20$ eV [18]. At the unoccupied part of the STS spectra, we can estimate the position of the HHB (0.25 eV), *B*3 (0.55 eV), *B*4 (0.80 eV), and $\Delta_{B3\text{-HHB}} = 0.30$ eV, $\Delta_{B4\text{-}B3} = 0.25$ eV. The values of the gaps estimated by Cho *et al.* [18] are equal to $\Delta_{B3\text{-HHB}} = 0.20$ eV and $\Delta_{B4\text{-}B3} = 0.20$ eV, respectively [18]. The extracted shape of the *dI*/*dV* (i.e., LDOS) is in accordance with the qualitative model of the CCDW phase given by Sato *et al.* [17]. In this model, the 5*d* density of states splits into three manifolds below the Fermi level derived from the Ta $5d_{z^2}$ orbitals and three manifolds above the Fermi level derived from the Ta $5d_{z^2}$, $5d_{zx}$, and $5d_{x^2-y^2}$ orbitals. The lower and upper Hubbard bands correspond to the Ta $5d_{z^2}$–derived bands which are symmetrically centered around the Fermi level and the distance between them defines Δ_{Mott}; see Fig. 8(a).

When the temperature is close to 293 K we observe the $1T$-TaS_2 surface in the NCCDW phase as proved by the STM and LEED measurements presented in Figs. 1(f) and 1(j); ARPES data are shown in Figs. 3(b), 3(e), and 4(b). The LDOS map recorded for the NCCDW phase shows a rather spatially homogeneous electronic structure with a distinct structure located at around 0.3–0.4 eV above the Fermi level and spatially formed on the surface; see Fig. 7(c). The *dI*/*dV* profile taken along the vertical cross section at the position marked by the arrow #1 in Fig. 7(c) is shown in Fig. 7(d). The presented *dI*/*dV* profile shows an asymmetric shape with the higher values of LDOS at the occupied part of the spectrum in comparison with the unoccupied part. Furthermore, a very distinct structure at energy close to 0.27 eV (r-HHB/MS) and a weak feature at around 0.9 eV (UB) above the Fermi level are clearly observed. In the case of room temperature, it was also possible to carry out STS measurements in the wider energy range (1.5 and 2 eV) around the Fermi level. However, in order to do that specific tunneling set points were chosen to avoid tunneling current saturation at the high bias voltages. These conditions resulted in the lower tunneling transmission coefficient leading to less pronounced features on the *dI*/*dV* curves as observed in Figs. 9(a) and 9(c). To overcome this problem the *dI*/*dV* spectra were normalized using a method where the differential conductance *dI*/*dV* is divided by the total conductance *I*/*V*, i.e., (*dI*/*dV*)/(*I*/*V*) [46]. The divergence problem (at small bias voltages) in the case of (*dI*/*dV*)/(*I*/*V*) was overcome by broadening $\Delta V = 1\,V$ to the *I*/*V* values [47]. The final results are presented in Figs. 9(b) and 9(d), where the average was performed over the 21 nm × 21 nm surface region.

In all normalized (*dI*/*dV*)/(*I*/*V*) spectra it is possible to observe very pronounced structures at the energy 0.26–0.27 eV (r-HHB/MS) and 0.80–0.95 eV (UB) above the Fermi level. Comparing the STS data with the ARIPES results collected at room temperature for the $\bar{\Gamma} - \bar{M}$ and $\bar{\Gamma} - \bar{K}$ directions [3] predicts that the r-HHB/MS structure can be ascribed to the unoccupied Ta $5d_{z^2}$–derived band. The energy position of this band estimated from the STS data is not too far from the energy derived from the normal incidence ARIPES experiment, which equals 0.5 eV. In our interpretation the observed r-HHB/MS structure can be treated as being reminiscent of the higher Hubbard band, which is observed in the CCDW phase at low temperature; see Fig. 7(b). However, this can also be treated as the metallic state typical of the ICCDW phase; see discussion devoted to STS on the ICCDW phase. Since the NCCDW phase is considered as a nearly hexagonal arrangement of the Mott insulating CCDW domains separated by the metallic ICCDW network both interpretations seem to be justified and feasible. The observed UB feature cor-

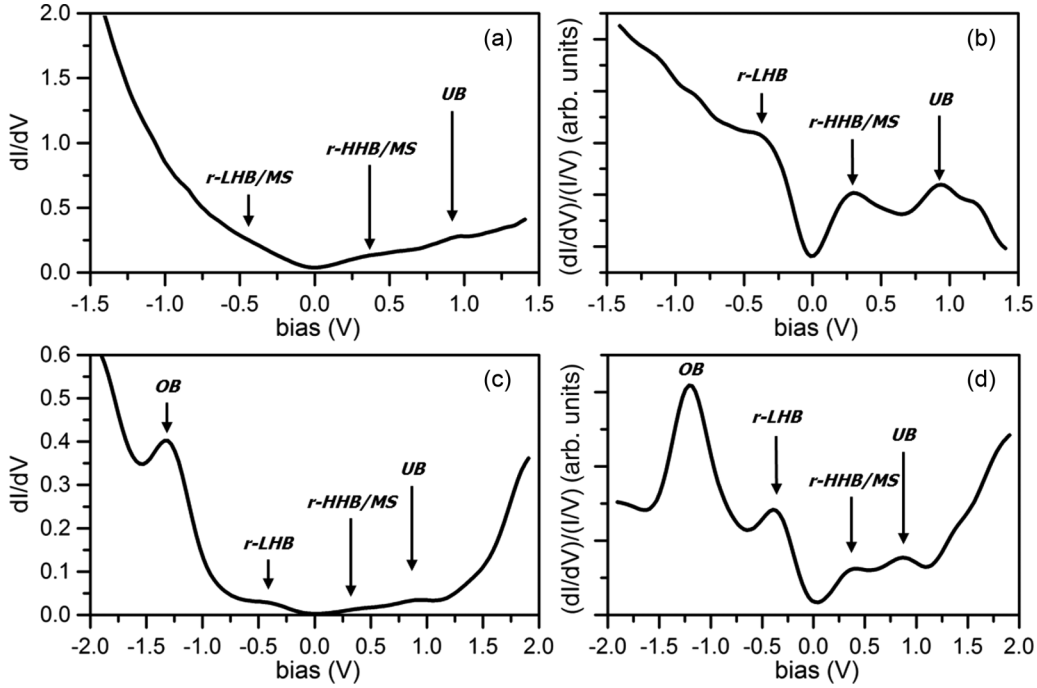

FIG. 9. (a), (b) *dI*/*dV* curve and its normalized form (*dI*/*dV*)/(*I*/*V*) for the NCCDW phase recorded at 1.5 V around the Fermi level. (c), (d) *dI*/*dV* curve and its normalized form (*dI*/*dV*)/(*I*/*V*) for the NCCDW phase recorded at 2 V around the Fermi level.

responds to the Ta $5d_{zx}$ and Ta $5d_{x^2-y^2}$–derived bands and can be associated with the *B*4 band observed in the CCDW phase [see Fig. 7(b)] and UB state for the NCCDW phase [see Fig. 7(d)]. The energies of the r-LHB and occupied band (OB) observed at the valence part of the spectra are close to 0.4 and 1.2 eV, respectively [Figs. 9(b) and 9(d)]. Similar to the case of unoccupied states the r-LHB state can be treated as being reminiscent of the lower Hubbard band observed in the CCDW phase; see Fig. 7(b). However, instead of the *B*1 and *B*2 bands and two gaps $\Delta_{\mathrm{CCDW},1}$, $\Delta_{\mathrm{CCDW},2}$ being the fingerprints for the CCDW phase, we observe only one distinct high-energy OB state. Since the energy of OB is higher than 1 eV below the Fermi level it may be caused by the presence of a parabolic band at the $\bar{\Gamma}$ point in the surface Brillouin zone as shown in our ARPES measurements; see Fig. 3 and 4. The intensity of this state may also be influenced by the lower-energy band at the $\bar{M}$ point. However, it should be mentioned that in tunneling spectroscopy measurements electronic states with $k_{\parallel} = 0$ ($\bar{\Gamma}$ point) have higher tunneling probability than the states with $k_{\parallel} \neq 0$ ($\bar{M}$ point). That is why the influence of this state seems to be rather negligible on the observed LDOS spectra. The schematic model of the DOS of the NCCDW phase is shown in Fig. 8(b).

Finally, we concentrate on the STS results recorded on the ICCDW phase observed at 400 K. The presented LDOS map and *dI*/*dV* profile [Figs. 7(e) and 7(f)] show the high value of LDOS at the Fermi level accompanied with a broad feature at an energy of about 0.20 eV below the Fermi level [metallic state (MS)]. The STS measurements performed at different regions on the surface proved that the energy of the MS varies considerably.

Particularly, it is possible to observe the edge of this metallic state (EMS) located at the unoccupied part of the spectra. The representative normalized LDOS maps and profiles of the (*dI*/*dV*)/(*I*/*V*) quantity measured at two different regions on the surface are presented in Fig. 10. In this case, the curves are taken from the vertical cross section at the position marked by the arrows #1 shown in Figs. 10(a) and 10(c). On the normalized LDOS maps, it is easy to observe the high value of LDOS at the Fermi level, which proves the metallic character of the investigated $1T$-TaS_2 surface in the ICCDW phase. This is also confirmed by the (*dI*/*dV*)/(*I*/*V*) curves [Figs. 10(b) and 10(d)] showing the high value of LDOS at the Fermi level accompanied with a very pronounced EMS located in the range of 0.15–0.20 eV at the unoccupied electronic states. The obtained STS results are in good agreement with our ARPES data showing lack of the energy gap below the Fermi level for the ICCDW phase. Furthermore, based on the dispersion relations for the ICCDW phase [Figs. 4(i) and 4(j)] the total and partial density of states were calculated and presented in Fig. 11. The conclusion from the presented data is straightforward; the density of states and partial density of states show a high value at the Fermi level. What is more, on the total DOS, partial DOS for electrons localized on Ta atoms, and partial DOS for total angular momentum, we observe a very distinct peak located at about 0.20 eV above the Fermi level. This value is in good agreement with our STS measurements showing very pronounced EMS located in the range of 0.15–0.20 eV above the Fermi level. The schematic model of the DOS structure of the ICCDW phase is shown in Fig. 8(c).

So far we have compared the tunneling spectra recorded for the CCDW, NCCDW, and ICCDW phases with the ARPES and ARIPES dispersion relations. It is tempting to carry on with such a comparison considering IEDCs. Firstly, the maxima ascribed to the LHB, r-LHB, MS, and OB on the LDOS measured by STS (Figs. 7, 9, and 10) might be correlated with the maxima which appeared on the IEDCs (Fig. 6). This is

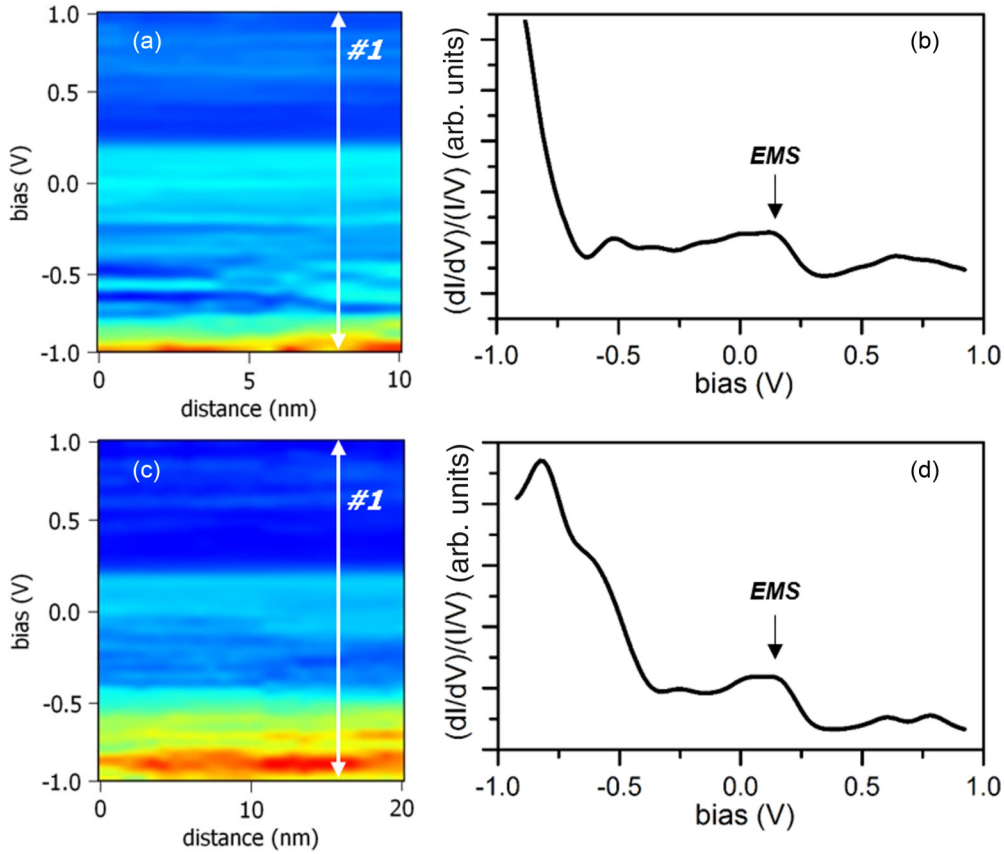

FIG. 10. (a), (c) Normalized LDOS map and (b), (d) $(dI/dV)/(I/V)$ curves recorded at 400 K for the ICCDW phase. On the LDOS map blue color corresponds to the very low value of LDOS, while red color corresponds to the very high value of LDOS.

especially well seen on the IEDCs integrated for the narrow wave-vector range around $\vec{k}_{\parallel} \approx 0$ presented in Fig. 6(a). This good agreement is caused by the fact that the STS technique is very sensitive to electronic states located in the center of the Brillouin zone. It is also possible to see weak maxima on the IEDC recorded at 130 K, which are related to the $B1$ and $B2$ states observed on the STS spectrum presented in Fig. 7(b). Furthermore, we observe the high intensity of the IED signal above the Fermi level at 400 K. This is a direct indication of the edge of the metallic state above the Fermi level observed by STS; see Figs. 10(b) and 10(d). For a comparison, we present IEDCs integrated for the wider wave-vector range: $-0.1\,\text{Å}^{-1}$ up to $1.0\,\text{Å}^{-1}$ [Fig. 6(b)]. As previously the spectra show very pronounced LHB, r-LHB, and MS states while only a weak OB state is observed. The case of IEDCs integrated in the wide wave-vector range is particularly interesting when compared with both our theoretical DFT calculations and ARPES measurements. This is because based on the disper-

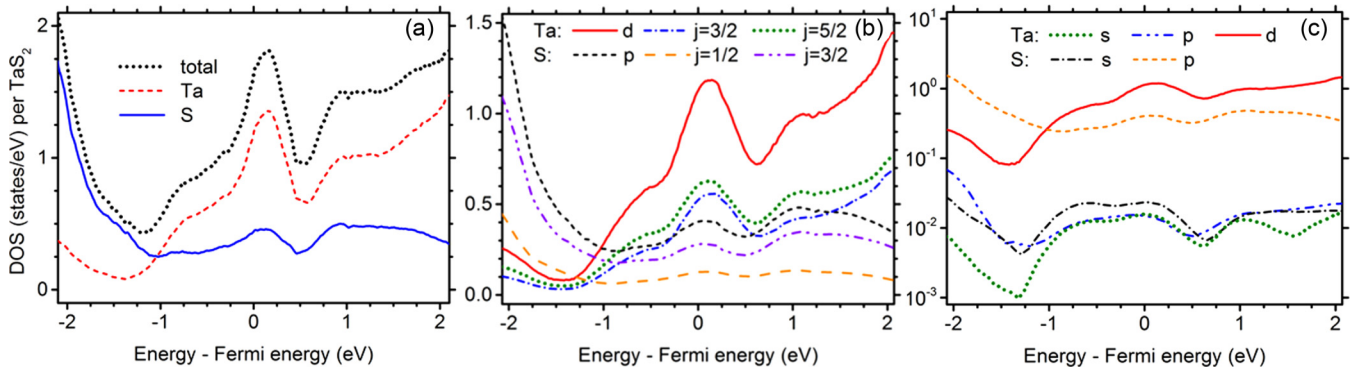

FIG. 11. Total and partial density of states calculated for bulk $1T$-TaS_2 without periodic lattice distortion representative for the presence of the ICCDW phase. The densities of states were calculated based on the band structure presented in Figs. 3(i) and 3(j). (a) Total density of states and partial density of states for electrons localized on Ta and S atoms. (b) Partial density of states for tantalum s, p, d orbitals and sulfur s, p orbitals. (c) Partial density of states in logarithmic scale for different total angular momentum.

sion relations for the ICCDW phase [Figs. 4(i) and 4(j)] the total and partial density of states were calculated in the wide wave-vector range and shown in Fig. 11.

IV. CONCLUSIONS

In summary, we have investigated the electronic structure of a UHV cleaved $1T$-TaS_2 crystal at different temperatures. The structure revealed by LEED and STM techniques at 110, 293, and 400 K proved the existence of the CCDW, NCCDW, and ICCDW phases, respectively.

The STS data recorded for the CCDW phase showed splitting of the Ta $5d$–derived band into three occupied submanifolds (LHB, $B1$, $B2$) separated by the energy gaps ($\Delta_{\mathrm{CCDW},1}$, $\Delta_{\mathrm{CCDW},2}$). The obtained results are in accordance with our ARPES data for the CCDW phase. At the unoccupied states, the STS revealed three unoccupied submanifolds (HHB, $B3$, $B4$) and energy gaps between them ($\Delta_{B3\text{-HHB}}$, $\Delta_{B4\text{-}B3}$). Our STS data for occupied and unoccupied states enabled us to estimate the Mott gap $\Delta_{\mathrm{Mott}} = 0.4$ eV defined as a distance between the lower and higher Hubbard bands. This value is comparable with the value estimated from the combined ARPES/ARIPES experiments and other STS data. The LDOS maps recorded for the CCDW phase show electronic structure heterogeneity considered in terms of changes of amplitude and energy position of the LDOS features along the position on the surface. It might be caused by the presence of surface defects or regions in which coexistence of different phases takes place.

We have shown the LDOS map and tunneling spectra in the wide energy range (1.5 and 2.0 eV) around the Fermi level for the NCCDW phase. Particularly, the STS results showed the reminiscence of the LHB (r-LHB, 0.4 eV) and HHB (r-HHB, 0.27 eV) bands. The state at energy 0.27 eV can also be treated as the metallic state (MS). The STS spectra showed a very pronounced electronic state for the occupied states (OB, 1.2 eV) associated with the parabolic band at the $\bar{\Gamma}$ point in the Brillouin zone. We also observed the electronic state at the unoccupied band (UB, 0.80–0.95 eV) corresponding to the Ta $5d_{zx}$ and Ta $5d_{x^2-y^2}$–derived bands. In contradiction to the CCDW, the LDOS map recorded for the NCCDW phase shows rather spatially homogeneous electronic structure with a very distinct state located at around 0.3–0.4 eV above the Fermi level ascribed to the r-HHB or MS states. The obtained STS data agree with the ARPES results for the NCCDW phase.

The STS data recorded on the ICCDW phase showed the high value of LDOS at the Fermi level and the very pronounced edge of the metallic state (EMS) located in the range of 0.15–0.20 eV at the unoccupied electronic band. This is also confirmed by LDOS maps recorded at different regions on the surface. The obtained results are consistent with the ARPES data showing lack of the energy gap below the Fermi level for the ICCDW phase.

Our experimental results agree well with our numerical calculations performed within the DFT formalism including SOC. Particularly, they confirm that the CCDW phase behaves as an insulator with the in-plane energy gap of 0.4 eV, and exhibits metallic properties in the out-of-plane direction. However, developing a fully accurate quantitative theory for the low-temperature CCDW phase would require taking into account a subtle and complex Hubbard physics, which governs the behavior of the system close to the Fermi level. This aim is highly challenging to reach within the present DFT approach as the noncollinear calculations must be made since the spin-orbit coupling plays an important role there. Our theoretical results are also suitable for the description of the ICCDW phase due to the fact that at higher temperatures the PLD is reduced compared to the CCDW phase. It was shown that the ICCDW phase is metallic in the in-plane directions, and it behaves as an insulator in the out-of-plane direction having a 0.5-eV gap. The band shapes and energies revealed by ARPES for the ICCDW phase were in accordance with a theoretical model without PLD. Both total and partial densities of states were proved to exhibit a maximum at 0.2 eV above the Fermi level. This value agrees with the STS measurements showing the very pronounced edge of the metallic surface state located in the range of 0.15–0.20 eV above the Fermi level.

ACKNOWLEDGMENT

The work was financially supported by The National Science Centre (Poland) under Grant No. 2015/19/B/ST3/03142.

[1] Q. H. Wang, K. Kalantar-Zadeh, A. Kis, J. N. Coleman, and M. S. Strano, Nat. Nanotechnol. **7**, 699 (2012).
[2] K. Rossnagel, J. Phys.: Condens. Matter **23**, 213001 (2011).
[3] R. Claessen, B. Burandt, H. Carstensen, and M. Skibowski, Phys. Rev. B **41**, 8270 (1990).
[4] F. Zwick, H. Berger, I. Vobornik, G. Margaritondo, L. Forró, C. Beeli, M. Onellion, G. Panaccione, A. Taleb-Ibrahimi, and M. Grioni, Phys. Rev. Lett. **81**, 1058 (1998).
[5] T. Pillo, J. Hayoz, H. Berger, M. Grioni, L. Schlapbach, and P. Aebi, Phys. Rev. Lett. **83**, 3494 (1999).
[6] T. Pillo, J. Hayoz, H. Berger, R. Fasel, L. Schlapbach, and P. Aebi, Phys. Rev. B **62**, 4277 (2000).
[7] T. Pillo, J. Hayoz, D. Naumović, H. Berger, L. Perfetti, L. Gavioli, A. Taleb-Ibrahimi, L. Schlapbach, and P. Aebi, Phys. Rev. B **64**, 245105 (2001).
[8] M. Bovet, S. van Smaalen, H. Berger, R. Gaal, L. Forró, L. Schlapbach, and P. Aebi, Phys. Rev. B **67**, 125105 (2003).
[9] M. Arita, H. Negishi, K. Shimada, F. Xu, A. Ino, Y. Takeda, K. Yamazaki, A. Kimura, S. Qiao, S. Negishi, M. Sasaki, H. Namatame, and M. Taniguchi, Physica B (Amsterdam, Neth.) **351**, 265 (2004).
[10] M. Bovet, D. Popović, F. Clerc, C. Koitzsch, U. Probst, E. Bucher, H. Berger, D. Naumović, and P. Aebi, Phys. Rev. B **69**, 125117 (2004).
[11] F. Clerc, C. Battaglia, M. Bovet, L. Despont, C. Monney, H. Cercellier, M. G. Garnier, P. Aebi, H. Berger, and L. Forró, Phys. Rev. B **74**, 155114 (2006).
[12] J. C. Petersen, S. Kaiser, N. Dean, A. Simoncig, H. Y. Liu, A. L. Cavalieri, C. Cacho, I. C. E. Turcu, E. Springate, F. Frassetto,

L. Poletto, S. S. Dhesi, H. Berger, and A. Cavalleri, Phys. Rev. Lett. **107**, 177402 (2011).
[13] R. Ang, Y. Tanaka, E. Ieki, K. Nakayama, T. Sato, L. J. Li, W. J. Lu, Y. P. Sun, and T. Takahashi, Phys. Rev. Lett. **109**, 176403 (2012).
[14] S. Hellmann, T. Rohwer, M. Kalläne, K. Hanff, C. Sohrt, A. Stange, A. Carr, M. M. Murnane, H. C. Kapteyn, L. Kipp, M. Bauer, and K. Rossnagel, Nat. Commun. **3**, 1069 (2012).
[15] C. Sohrt, A. Stange, M. Bauer, and K. Rossnagel, Faraday Discuss. **171**, 243 (2014).
[16] T. Ritschel, J. Trinckauf, K. Koepernik, B. Büchner, M. v. Zimmermann, H. Berger, Y. I. Joe, P. Abbamonte, and J. Geck, Nat. Phys. **11**, 328 (2015).
[17] H. Sato, M. Arita, Y. Utsumi, Y. Mukaegawa, M. Sasaki, A. Ohnishi, M. Kitaura, H. Namatame, and M. Taniguchi, Phys. Rev. B **89**, 155137 (2014).
[18] D. Cho, Y.-H. Cho, S.-W. Cheong, K.-S. Kim, and H. W. Yeom, Phys. Rev. B **92**, 085132 (2015).
[19] S. Qiao, X. Li, N. Wang, W. Ruan, C. Ye, P. Cai, Z. Hao, H. Yao, X. Chen, J. Wu, Y. Wang, and Z. Liu, Phys. Rev. X **7**, 041054 (2017).
[20] Y. Fujisawa, T. Shimabukuro, H. Kojima, K. Kobayashi, S. Ohta, T. Machida, S. Demura, and H. Sakata, J. Phys. Soc. Jpn. **86**, 113703 (2017).
[21] D. Cho, S. Cheon, K.-S. Kim, S.-H. Lee, Y.-H. Cho, S.-W. Cheong, and H. W. Yeom, Nat. Commun. **7**, 10453 (2016).
[22] L. Ma, C. Ye, Y. Yu, X. F. Lu, X. Niu, S. Kim, D. Feng, D. Tománek, Y.-W. Son, X. H. Chen, and Y. Zhang, Nat. Commun. **7**, 10956 (2016).
[23] W. Kohn and L. J. Sham, Phys. Rev. **140**, A1133 (1965).
[24] P. Giannozzi, S. Baroni, N. Bonini, M. Calandra, R. Car, C. Cavazzoni, D. Ceresoli, G. L. Chiarotti, M. Cococcioni, I. Dabo, A. Dal Corso, S. de Gironcoli, S. Fabris, G. Fratesi, R. Gebauer, U. Gerstmann, C. Gougoussis, A. Kokalj, M. Lazzeri, L. Martin-Samos *et al.*, J. Phys.: Condens. Matter **21**, 395502 (2009).
[25] P. Giannozzi, O. Andreussi, T. Brumme, O. Bunau, M. Buongiorno Nardelli, M. Calandra, R. Car, C. Cavazzoni, D. Ceresoli, M. Cococcioni, N. Colonna, I. Carnimeo, A. Dal Corso, S. de Gironcoli, P. Delugas, R. A. DiStasio, A. Ferretti, A. Floris, G. Fratesi, G. Fugallo *et al.*, J. Phys.: Condens. Matter **29**, 465901 (2017).
[26] G. Kresse and D. Joubert, Phys. Rev. B **59**, 1758 (1999).
[27] J. P. Perdew, K. Burke, and M. Ernzerhof, Phys. Rev. Lett. **77**, 3865 (1996).
[28] A. Spijkerman, J. L. de Boer, A. Meetsma, G. A. Wiegers, and S. van Smaalen, Phys. Rev. B **56**, 13757 (1997).
[29] I. Horcas, R. Fernández, J. M. Gómez-Rodríguez, J. Colchero, J. Gómez-Herrero, and A. M. Baro, Rev. Sci. Instrum. **78**, 013705 (2007).
[30] J. R. Duffey, R. D. Kirby, and R. V. Coleman, Solid State Commun. **20**, 617 (1976).
[31] R. He, J. Okamoto, Z. Ye, G. Ye, H. Anderson, X. Dai, X. Wu, J. Hu, Y. Liu, W. Lu, Y. Sun, A. N. Pasupathy, and A. W. Tsen, Phys. Rev. B **94**, 201108 (2016).
[32] O. R. Albertini, R. Zhao, R. L. McCann, S. Feng, M. Terrones, J. K. Freericks, J. A. Robinson, and A. Y. Liu, Phys. Rev. B **93**, 214109 (2016).
[33] M. Yoshida, Y. Zhang, J. Ye, R. Suzuki, Y. Imai, S. Kimura, A. Fujiwara, and Y. Iwasa, Sci. Rep. **4**, 7302 (2015).
[34] M. Yoshida, R. Suzuki, Y. Zhang, M. Nakano, and Y. Iwasa, Sci. Adv. **1**, e1500606 (2015).
[35] Y. Yu, F. Yang, X. F. Lu, Y. J. Yan, Y.-H. Cho, L. Ma, X. Niu, S. Kim, Y.-W. Son, D. Feng, S. Li, S.-W. Cheong, X. H. Chen, and Y. Zhang, Nat. Nanotechnol. **10**, 270 (2015).
[36] See Supplemental Material at http://link.aps.org/supplemental/10.1103/PhysRevB.98.195425 for angle-resolved photoemission spectroscopy measurements.
[37] S. Vogelgesang, G. Storeck, J. G. Horstmann, T. Diekmann, M. Sivis, S. Schramm, K. Rossnagel, S. Schäfer, and C. Ropers, Nat. Phys. **14**, 184 (2017).
[38] B. Burk, R. E. Thomson, A. Zettl, and J. Clarke, Phys. Rev. Lett. **66**, 3040 (1991).
[39] X. L. Wu, J. Vac. Sci. Technol. B Microelectron. Nanometer Struct.–Process., Meas., Phenom. **9**, 1044 (1991).
[40] R. E. Thomson, U. Walter, E. Ganz, J. Clarke, A. Zettl, P. Rauch, and F. J. DiSalvo, Phys. Rev. B **38**, 10734 (1988).
[41] X. L. Wu and C. M. Lieber, Phys. Rev. Lett. **64**, 1150 (1990).
[42] R. E. Thomson, B. Burk, A. Zettl, and J. Clarke, Phys. Rev. B **49**, 16899 (1994).
[43] X.-L. Yu, D.-Y. Liu, Y.-M. Quan, J. Wu, H.-Q. Lin, K. Chang, and L.-J. Zou, Phys. Rev. B **96**, 125138 (2017).
[44] R. Manzke, O. Anderson, and M. Skibowski, J. Phys. C: Solid State Phys. **21**, 2399 (1988).
[45] T. Greber, O. Raetzo, T. J. Kreutz, P. Schwaller, W. Deichmann, E. Wetli, and J. Osterwalder, Rev. Sci. Instrum. **68**, 4549 (1997).
[46] R. M. Feenstra, J. A. Stroscio, and A. P. Fein, Surf. Sci. **181**, 295 (1987).
[47] R. M. Feenstra, Phys. Rev. B **50**, 4561 (1994).